

Article

In Situ Investigations on Stress and Microstructure Evolution in Polycrystalline Ti(C,N)/ α -Al₂O₃ CVD Coatings under Thermal Cycling Loads

José García ^{1,*}, Maiara Moreno ², Wei Wan ¹, Daniel Apel ³, Haroldo Pinto ² , Matthias Meixner ³, Manuela Klaus ³ and Christoph Genzel ³

¹ AB Sandvik Coromant, R&D Material and Processes, SE 12680 Stockholm, Sweden; wei.wan@sandvik.com

² Department of Materials Engineering, University of São Paulo, SP 13563-120 São Carlos, Brazil; morenomaiara95@gmail.com (M.M.); haroldo@sc.usp.br (H.P.)

³ Abteilung Mikrostruktur-und Eigenspannungsanalyse, Helmholtz-Zentrum Berlin für Materialien und Energie GmbH, D-12489 Berlin, Germany; daniel.apel@helmholtz-berlin.de (D.A.); matthias.meixner@helmholtz-berlin.de (M.M.); klaus@helmholtz-berlin.de (M.K.); genzel@helmholtz.de (C.G.)

* Correspondence: jose.garcia@sandvik.com

Abstract: The stress behavior and the associated microstructure evolution of industrial Ti(C,N)/ α -Al₂O₃ coatings subjected to thermal cycling are investigated by in situ energy dispersive synchrotron X-ray diffraction and transmission electron microscopy. Temperature-dependent stresses and changes in microstructural parameters (domain size and microstrain) are analyzed by in situ measurements at different temperatures between 25 and 800 °C, both in the heating up and cooling down step, including several thermal cycles. Transmission electron microscopy is used to evaluate defects before and after the thermal treatment. The introduction of high compressive stresses in α -Al₂O₃ by top-blasting is connected to a high defect density at the basal planes of the alumina layer. The stress relaxation of the alumina layer at high temperatures is associated with a successive annihilation of defects until a reversible temperature-dependent stress condition is set. Top-blasting does not change the initial microstructure and residual stress of the Ti(C,N) layer. Ti(C,N) shows a cyclic stress behavior associated with the heat treatment and an elastic deformation behavior in the temperature range investigated.

Keywords: Ti(C,N)/ α -Al₂O₃ CVD coatings; residual and thermal stresses; synchrotron X-ray diffraction; TEM characterization; microstructure evolution



Citation: García, J.; Moreno, M.; Wan, W.; Apel, D.; Pinto, H.; Meixner, M.; Klaus, M.; Genzel, C. In Situ Investigations on Stress and Microstructure Evolution in Polycrystalline Ti(C,N)/ α -Al₂O₃ CVD Coatings under Thermal Cycling Loads. *Crystals* **2021**, *11*, 158. <https://doi.org/10.3390/cryst11020158>

Academic Editor: Shujun Zhang

Received: 12 January 2021

Accepted: 1 February 2021

Published: 4 February 2021

Publisher's Note: MDPI stays neutral with regard to jurisdictional claims in published maps and institutional affiliations.



Copyright: © 2021 by the authors. Licensee MDPI, Basel, Switzerland. This article is an open access article distributed under the terms and conditions of the Creative Commons Attribution (CC BY) license (<https://creativecommons.org/licenses/by/4.0/>).

1. Introduction

Metal part components in the automotive and aerospace industry are manufactured to their final shape with cemented carbide coated tools [1]. WC-Co-based cemented carbides coated with Ti(C,N)/ α -Al₂O₃ multilayers of few micrometers by chemical vapor deposition (CVD) represent more than 50% of the total world market. The reason for this is the outstanding balance of hardness and toughness of cemented carbides [2] combined with the excellent chemical/heat resistance (provided by the aluminum oxide layer) and wear resistance (provided by the carbonitride layer) of the coatings [3]. Many machining applications usually involve interrupted cutting conditions; hence, the design of coated systems that withstand cycling thermomechanical loads is vital to maximize performance and productivity in metal cutting. However, due to the manufacturing process (CVD at 1000 °C) and the differences in coefficient of thermal expansion (CTE) between the carbide substrate and the coating layers (typically $CTE_{\text{film}} - CTE_{\text{carbide}} > 3 \times 10^{-6} \text{ K}^{-1}$), a network of microcracks is formed in the CVD coating upon cooling to room temperature (RT). Hence, during interrupted machining, thermomechanical wear-induced comb cracks form on existing CVD cooling microcracks, which leads to limited performance and failure of the

tools [4]. One way of extending the tool life of cemented carbide CVD-coated inserts is to introduce high compressive residual stresses (> -1 GPa) in the α -Al₂O₃ layer by top-blasting (impacting the surface with high energy particles). Compressive stresses retard the opening of microcracks, which leads to the formation of thermomechanical cracks [4–7].

There are several reports on stress behavior of multilayer polycrystalline wear resistant CVD layers at varying thermal conditions. However, a complete description of the correlation between stress behavior of multilayer coatings under thermal cycling and the microstructural changes associated with the development of residual stresses needs further understanding. Stress depth profiles, average stresses and microstructure development on single titanium nitride (TiN) layers deposited on cemented carbide in a temperature range of 25–1100 °C were reported by Bartosik et al. [8]. It was observed that top-blasting influenced the surface microstructure of the TiN film and that the residual stresses are relaxed already at low temperatures in the heating up part of the cycling step. Upon cooling down to 25 °C (RT) from the CVD deposition temperature, tensile residual stresses evolve and are partially relaxed by crack formation. In a previous investigation by the authors of this work, the temperature dependence of thermal stresses for titanium carbonitride Ti(C,N) layers deposited by CVD on functionally graded cemented carbides was reported [9]. Tensile residual stresses at RT evolved into compressive stresses at 800 °C. Relaxation of compressive residual stresses (originating from top-blasting with alumina particles) was measured after heat treatment at 800 °C. Furthermore, residual stresses in the as-coated condition were below the expected calculated theoretical values, again associated with cracking of the layer during cooling from the CVD process. A plasticity model using Finite Element Modeling (FEM) was applied to match the measured residual and thermal stress values and the theoretical calculations, which may imply that the carbonitride layer undergoes considerable plastic deformation during the thermal cycling treatment. Complementary to the study on top-blasting was the work reported on the effect of shot peening on CVD-coated cutting inserts [10]. The study revealed the introduction of high compressive residual stresses by peening in both the α -Al₂O₃ and Ti(C,N) layer and the cemented carbide substrate, together with closure of CVD cooling cracks.

Recently, the thermal crack formation in Ti(C,N)/ α -Al₂O₃ bilayer coatings grown by thermal CVD on WC-Co substrates with varied Co content has been investigated [11,12]. It was concluded that increased Co contents in the substrate reduced the CTE mismatch between the carbide and the coating layers, even suppressing the formation of CVD cooling crack networks for Co contents above 12 wt%. Additionally, residual stress of the bilayer coatings was determined using X-ray diffraction. A secondary stress relaxation mechanism (undefined as described by the authors, and probably associated with the binder phase transformation of the cemented carbide, which was not visible in dilatometry measurements [10]) in the Ti(C,N) film of the bilayer coatings was suggested to account for discrepancies between stresses calculated by FEM and those determined by XRD in the temperature range RT–1000 °C. A common observation of all previous works [8–12] is the reversible behavior of stresses for Ti(C,N) below the deposition temperature; however, if the heat treatment surpasses deposition temperature (890 °C), then the formation of additional thermal microcracks is suggested for a kink in stresses at around 450 °C [11,12]. However, the assumptions of relaxation due to microcracking and plasticity effects (of the carbonitride coating layers [9] or the Co binder phase of cemented carbides [11,12]) may not be conclusive to explain the observed stress variations in CVD coatings and their impact on the performance of industrial coated cutting tools.

To elucidate which microstructural changes are associated with the cycling stress evolution of Ti(C,N)/ α -Al₂O₃ CVD multilayers, we conducted studies on residual and thermal stresses for several thermal cycles on an industrial cutting insert with a flat surface in as-coated and top-blasted conditions using in situ energy dispersive synchrotron X-ray diffraction at temperature steps of 200 °C in the range 25–800 °C, both in heating and cooling ramps. Information about in situ microstructural changes taking place in the coating layers and its correlation to the stress behavior was obtained by analyzing the

integral breadth of the diffraction lines at different temperatures. The microstructural changes determined by X-ray diffraction were correlated with microstructure analysis of the multilayers (before and after treatment) using scanning TEM (STEM).

2. Materials and Methods

2.1. Samples

The CVD α -Al₂O₃/Ti(C,N) coating system was deposited in a hot-wall industrial reactor onto cemented carbides substrates (WC-6% Co) produced by state-of-the-art powder metallurgy sintering techniques. The dimensions of the quadratic substrate are 10 × 10 × 5 mm thickness. The insert geometry was selected with a flat surface to avoid geometry effects on stress analysis. Flat surfaces are needed to avoid shadow effects at high grazing angles that may affect the measurement. Additionally, if the irradiated surface area is too small, then the measurement time increases dramatically, making the in situ analysis less feasible. Additionally, edge rounding of 35 μ m was performed on all edges of the substrate to avoid concentration of stresses due to sharp edges. A thin starting layer of TiN was first deposited, followed by a Ti(C,N) layer from a gas mixture TiCl₄-CH₃CN-H₂ at 870 °C, a Ti(C,N,O) bonding layer and an α -Al₂O₃ top-layer using a gas mixture of AlCl₃-ClH₂-CO₂ at a temperature of 1000 °C. After deposition, some samples were subjected to a wet top-blasting process (pressure 2 bars for 60 s) with microparticles of alumina (particle size of 250 μ m) using an injector-type system in commercial industrial blasting equipment.

2.2. Residual Stress Analysis in the Coating Layers

Residual stresses in the as-deposited and as-blasted samples were analyzed prior to the heat treatment, whereas the thermal stresses were analyzed in situ, both using synchrotron radiation. The energy-dispersive X-ray diffraction (EDXRD) experiments were carried out at the Material Science Beamline energy-dispersive diffraction (EDDI) at the storage ring BESSY in Berlin, Germany [13,14]. The main advantage of the energy-dispersive diffraction method is that complete diffraction spectra with a multitude of diffraction lines E^{hkl} are obtained within short measurement times under a fixed diffraction angle 2θ (symmetrical ψ -Mode), which can be chosen freely to adapt the measurement conditions to the specific sample design and/or -environment. This allows for the simultaneous analysis of residual stresses and microstructural properties of all coating layers as well as the substrate material. However, in order to reduce the measurement time per temperature step, a limited number of inclination angles, necessary for the residual stress analysis, were chosen. This is performed at the expense of information needed to analyze possible residual stress gradients inside of the coating layers [15,16], which is why the residual stresses reported in this paper are average stresses over the film thickness. EDXRD does not allow for a separation of the diffraction lines originating from the TiN starting layer and the Ti(C,N,O) bonding layer, since they superpose with the diffraction lines of the main Ti(C,N) layer. The sample was mounted on a goniometer which was aligned with the primary beam. The sample was then simply aligned using the x-y-z-table. The correct sample height was adjusted by laser triangulation and verified by intensity measurements. In the present case, the gauge volume was not defined by the aperture of the slits in the primary and diffracted beam but was given by irradiated surface area (approximately 0.5 × 6.4 mm² times the thickness of the individual layers).

The experimental parameters used at EDDI beamline are shown in Table 1.

The thermal residual stresses were measured at different temperatures in situ by heating the sample in an Anton-Paar furnace under flowing argon. The initial measurement was performed at room temperature of 25 °C (RT). A thermocouple was mounted on top of the sample to track the temperature level. Then, the samples were heated (heating rate 500 K/min) at temperature steps of 100–200 °C, and the residual stresses were measured in situ. Once the target temperature was reached, usually a short period of time was considered (30–60 s) until the temperature was stable enough to begin with the X-ray measurement. Each measurement took approximately 10 min. The temperature remained stable during

the measurement time. The maximum temperature was 800 °C. The same procedure was applied during cooling down until reaching room temperature again. In some samples, this cycling procedure was repeated several times.

Table 1. Experimental parameters.

Primary Beam	0.5 × 0.5 mm ²
Absorber	-
Secondary Optics	double slit system 0.03 × 8 mm ² (equatorial × axial), Δ2θ < 0.01
Diffraction Angle	2θ = 9°
XSA-Mode	symmetrical ψ-Mode (reflection), ψ = 0° to 77°, Δ(sin ² ψ) = 0.1
Detector	Low energy solid state Ge detector (Canberra Model GL0110)
Counting Time	100 s
Calibration	gold powder (standard specimen on glass plate)
Energy Range	10–80 keV

The fundamental equation of stress analysis using XRD was applied to determine the thermal stresses in the Ti(C,N)/α-Al₂O₃ coatings. For a given *hkl* diffraction line, the relation between the elastic strain (ϵ^{hkl}) at different inclination angles ψ and $\sin^2\psi$ is presented in Equation (1), according to the description of Noyan et al. [17]

$$\epsilon_{\psi}^{hkl} = \frac{d_{\psi}^{hkl} - d_0^{hkl}}{d_0^{hkl}} = \frac{1}{2} S_2^{hkl} \sigma_{\parallel} \sin^2\psi + 2S_1^{hkl} \sigma_{\parallel} \quad (1)$$

where d_{ψ}^{hkl} is the lattice spacing to be determined and d_0^{hkl} denotes the lattice spacing of the strain-free material. S_1^{hkl} and $\frac{1}{2}S_2^{hkl}$ are the diffraction elastic constants (DEC) valid for quasi-isotropic polycrystalline materials. They are independent of the measurement direction with respect to the sample system but reflect the elastic anisotropy of the crystallites the material consists of. Equation (1) holds for a biaxial stress state of rotational symmetry, which is described by the in-plane stress component σ_{\parallel} [18]. The rotational symmetry has been proven in preliminary ex-situ investigations on coating systems of similar/same design.

The measured $d_{\psi}^{hkl} - \sin^2\psi$ distributions proved to be almost linear within the experimentally caused scattering. Therefore, X-ray stress analysis using Equation (1) can be performed by applying the $\sin^2\psi$ method [19] to the obtained $d_{\psi}^{hkl} - \sin^2\psi$ data sets. In the present case, the residual stress analysis on the two layers was performed for the diffraction lines summarized in Table 2, and the average of the resulting stress values was taken to monitor the stress evolution during thermal cycling.

Table 2. Diffraction elastic constants for the investigated layers. The diffraction elastic constants (DEC) were calculated by the Eshelby–Kröner model [20,21] using the respective single crystal elastic constants. For the stress evaluation in the Ti(C,N) layer, it is noted that the DEC for Titanium carbide (TiC) are very similar to those for TiN. Thus, an average of these values was used for the Ti(C,N) layer.

Component	Hkl	S_1^{hkl} [×10 ⁻⁶ MPa ⁻¹]	$\frac{1}{2}S_2^{hkl}$ [×10 ⁻⁶ MPa ⁻¹]
α-Al ₂ O ₃	012/024	-0.685	3.36
Ti(C,N)	200	-0.425	2.665
	220	-0.465	2.795

A comparison of the experimentally obtained residual stress values (σ_{\parallel}) and the theoretical values (σ_{th}) was made. Since the magnitude of the total coating thickness is of micrometers (~9 μm) compared to the bulk size (5000 μm), it can be assumed that the coating is in a plane-state of residual stress and that the theoretical stress value of each

single layer can be assumed to be independent of each other in the multilayer [22]. Hence, the magnitude of the thermal residual stress depends on the elastic modulus of the coating, the CTE of the layers and substrate, as well as the temperature variation. Thus, the thermal residual stress in the coating layers can be approximated as:

$$\sigma_{th} = \frac{E_L}{(1 - \nu_L)} \times (CTE_S - CTE_L) \times (T - T_{max}) \quad (2)$$

where σ_{th} is the thermal residual stress, E_L is the Young's modulus of the layer, ν_L is the poisson coefficient of the layer, T is the temperature and T_{max} is the maximum temperature of the deposition (1050 °C), CTE_S is the thermal expansion coefficient for the substrate and CTE_L is the thermal expansion coefficient of the layer. With these relations, it is possible to evaluate the theoretical values of the thermal residual stresses for the α -Al₂O₃ and Ti(C,N) layers. Table 3 presents the elastic and thermal properties for the cemented carbide and polycrystalline coatings used to calculate the thermal residual stresses [23–29]. For the calculation at different temperatures, a linear temperature dependence of the CTE and Young's modulus of Ti(C,N) [27,28] and α -Al₂O₃ [26,29] in the temperature range 25–800 °C was assumed.

Table 3. Elastic and thermal properties for substrate and coating layers.

Substrate/Coating Layer	Young's Modulus (GPa)	Poisson Coefficient, ν	Average CTE (20–800 °C) (10 ⁻⁶ /K)	Film Thickness (μm)
WC-Co	620 ± 20 [23]	0.22 [23]	5.7 [23]	-
α -Al ₂ O ₃	440 ± 20 [24]	0.22 [25]	a: 8.4/c: 9.0 [26]	4.5
Ti(C,N)	450 ± 20 [27]	0.19 [25]	9.0 [28]	4.5

2.3. Microstrain and Domain Analysis

Energy-dispersive X-ray diffraction was used to evaluate microstructural parameters, i.e., domain size and microstrain, in the as-coated and top-blasted conditions and their temperature dependency by analyzing the size and strain broadening of the diffraction lines based on the single-line method [30]. The diffraction lines were described using a pseudo-Voigt function:

$$pV(E) = \eta \cdot \Gamma_L(E) + (1 - \eta) \Gamma_G(E) \quad (3)$$

where η is the mixing parameter ($0 \leq \eta \leq 1$), and Γ_L and Γ_G depict the energy-dependent Lorentz and Gauss profiles of the full width at half maximum (FWHM) Γ . E is the fitted energy position of the respective diffraction line hkl. After correcting the measured values Γ_L and Γ_G with regard to the instrumental broadening and converting them to integral breadths according to the following equations [31]:

$$\frac{\beta_L}{\beta} = 2.0207 - 0.4803 \cdot \phi - 1.7756 \cdot \phi^2 \quad (4)$$

$$\frac{\beta_G}{\beta} = 0.6420 + 1.4187 \left(\phi - \frac{2}{\pi} \right)^{1/2} - 2.2043 \cdot \phi + 1.8706 \cdot \phi^2 \quad (5)$$

where β is the measured integral breadth, β_L and β_G the Lorentz and Gauss part of the integral breadth and $\phi = \frac{\Gamma}{\beta}$, it is possible to calculate the domain size D_V and the microstrain ϵ using the following equations [32]:

$$D_V = \frac{K \cdot hc}{2 \cdot \beta_L \sin \theta_0} = \frac{K \cdot 6.199 \left[\text{keV} \cdot \text{Å} \right]}{\beta_L [\text{keV}] \sin \theta_0} \quad (6)$$

$$e = \frac{\beta_G(E)[keV]}{2E} \quad (7)$$

where K is the Scherrer constant (close to unity), h the Planck's constant, c the speed of light, θ_0 the diffraction angle, E the energy and β_s and β_D are the integral breadths of the size and strain broadened line profiles, respectively.

2.4. Microstructure Characterization

Microstructure characterization was carried out using field-emission gun (FEG) scanning electron microscopy (SEM), Helios 40. To prepare lamella samples for TEM observations, cross-sectional slices of about 0.5 mm in thickness were cut from the insert by using a precision cutter and then mechanically polished on both sides to a thickness of around 30–50 μm . The samples were then moved to a dual-beam focused ion beam (FIB) instrument (Thermo-Fisher-Scientific Helios 650) for further polishing by ion beam. A protective Pt layer about 2 μm in thickness was first deposited on top of the $\alpha\text{-Al}_2\text{O}_3$ layer. The slices were then polished with ion beams at 30 kV and final low-kV polishing was performed at 2 kV. TEM observations, which included electron diffraction, scanning TEM (STEM) imaging and weak-beam dark-field (WBDF) imaging, were made on a double-corrected Thermo-Fisher-Scientific Titan G2 microscope operated at 300 kV. For the best visibility of the crystalline defects, dark-field scanning TEM (STEM) images were taken at a camera distance of 73 mm from crystal grains tilted into low-index zone axes, as described in [33].

3. Results and Discussion

3.1. SEM Microstructure Analysis

A cross-section image of the tip of the CVD coated cemented carbide investigated is shown in Figure 1a. The good adhesion of the Ti(C,N) and $\alpha\text{-Al}_2\text{O}_3$ layers to the WC-Co substrate are clearly visible. No pores or defects were found in the coatings (see included SEM image at higher magnification). A fracture image showing the polycrystalline layers with a larger magnification is shown in Figure 1b consisting of a thin TiN starting layer of 0.4 μm followed by a Ti(C,N) layer of 4.5 μm , a Ti(C,N,O) bonding layer (BL) and a $\alpha\text{-Al}_2\text{O}_3$ top-layer of 4.5 μm . The top surface of the as-deposited coating (Figure 1c) shows the typical topography of Al_2O_3 grains, together with a regular microcrack network (indicated by white arrows), which formed during the cooling step of the CVD process due to CTE differences between the coating layers and the cemented carbide substrate as reported in [4,12,34,35]. The averaged surface roughness (Rz) was $0.6 \pm 0.05 \mu\text{m}$. The top-blasted surface (not shown in this figure) presented a reduced roughness of $Rz = 0.2 \pm 0.05 \mu\text{m}$, which is an expected value based on previous works [35].

3.2. Synchrotron X-ray Stress Analysis

Results of the in situ stress evolution during two thermal cycles for the Ti(C,N)/ $\alpha\text{-Al}_2\text{O}_3$ system in the as-coated condition are presented in Figure 2a. Stresses were analyzed in temperature steps of 200 $^\circ\text{C}$. For $\alpha\text{-Al}_2\text{O}_3$, stresses reduce constantly from 500 (initial as-coated value at RT1) to -180 MPa at 800 $^\circ\text{C}$. During cooling down to RT2, the stresses evolve to tensile residual stresses reaching almost the same tensile value of 500 MPa as measured at RT1. In the second heat treatment up to 800 $^\circ\text{C}$, stresses evolve again to compressive residual stresses (-50 MPa), which is slightly below the value for the first heat step.

For the Ti(C,N) layer, a similar stress cycling behavior as for $\alpha\text{-Al}_2\text{O}_3$ was observed. At RT1, a tensile residual stress value of 500 MPa was determined; by increasing the temperature to 800 $^\circ\text{C}$, compressive stresses of -200 MPa were estimated. During the second thermal cycle (RT2–800 $^\circ\text{C}$ –RT3), the stress values for Ti(C,N) were the same as for the first thermal cycle, also showing a reversible cycling behavior with values of the same magnitude.

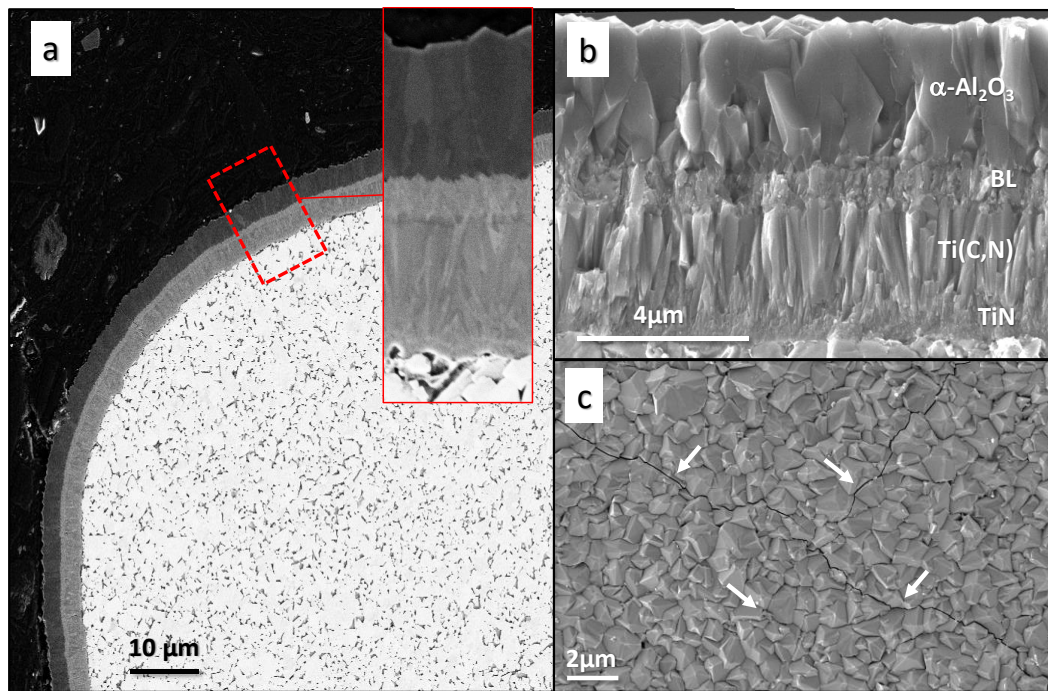


Figure 1. SEM images of (a) polished cross-section of CVD coated carbide insert tip together with highlighted high resolution SEM image; (b) cross-section fracture of the polycrystalline CVD multilayer; (c) top-view SEM image showing α - Al_2O_3 crystal morphology and microcrack network (white arrows).

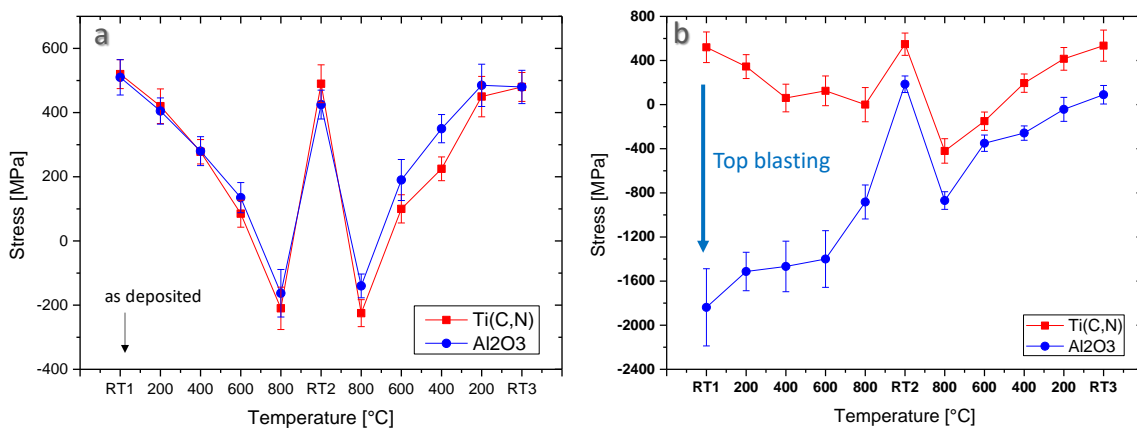


Figure 2. Temperature-dependent stress evolution during two thermal cycles for the $\text{Ti}(\text{C},\text{N})/\alpha\text{-Al}_2\text{O}_3$ system in: as-coated condition (a) and top-blasted condition (b).

Figure 2b presents the in situ determined stress values for the same system in top-blasted condition. The main difference is observed for the $\alpha\text{-Al}_2\text{O}_3$ layer, which presents compressive residual stresses in the as-blasted condition at RT1, a value of -1800 MPa. The compressive stress is present in the first heating step (-900 MPa at 800 °C) but decreases constantly during the cooling step to RT2 reaching tensile residual stress (200 MPa). In the second heat treatment up to 800 °C, stresses evolve to compressive stresses of -900 MPa again. During the last cooling step (800 – 200 °C), the compressive stresses evolve into tensile residual stresses. Compared to the stress evolution for the as-coated condition, it is observed that the stresses in the 2nd cycle are below those observed for the as-coated condition, which may indicate that the introduction of compressive stresses due to top-blasting cannot be completely released in this first temperature cycle.

For the Ti(C,N) layer in top-blasted condition, the initial residual stress (RT1) is of tensile type and same magnitude as for the as-coated condition (+500 MPa), indicating that the top-blasting did not cause a considerable effect on the residual stress of the carbonitride layer. In the following thermal cycles, the Ti(C,N) evolves from tensile (RT) to compressive stresses (at high temperature). It is worth noting that already in the second heating cycle, both the Ti(C,N) and the α -Al₂O₃ layers present a similar cycling stress behavior.

A summary of results for 5 thermal cycles is presented in Figure 3. The thermal cycling behavior of both Ti(C,N) and α -Al₂O₃ (top-blasted system) is plotted as function of temperature. The evolution of stresses in the α -Al₂O₃ layer shows a compressive residual stress at room temperature after top-blasting (−1800 MPa), which evolves to a value of −900 MPa at 800 °C. After cooling down to RT in the 1st thermal cycle, the stresses evolve to tensile residual stresses of about +100 MPa. By repeating several thermal cycles (5) at the same temperature intervals ($\Delta T = 800$ °C), the stresses of the α -Al₂O₃ layer oscillates between tensile and compressive (the determined stress values of almost the same magnitude). This indicates that the α -Al₂O₃ layer presents two different stages: one consisting of stress relaxation of top-blasted-induced stresses in the first heating step, and a reversible tensile–compressive–tensile behavior of the same magnitude for the alternating subsequent cycles. The relaxation of residual stresses in post-treated α -Al₂O₃ has also been observed previously in other studies [4,6,36] and the reversible behavior for one thermal cycle in [4,12]. The results of this study on several thermal cycles show that the top-blasting effect decreases continuously with the increased number of thermal cycles, namely, −900 to −450 MPa at 800 °C and +50 to +350 MPa at RT.

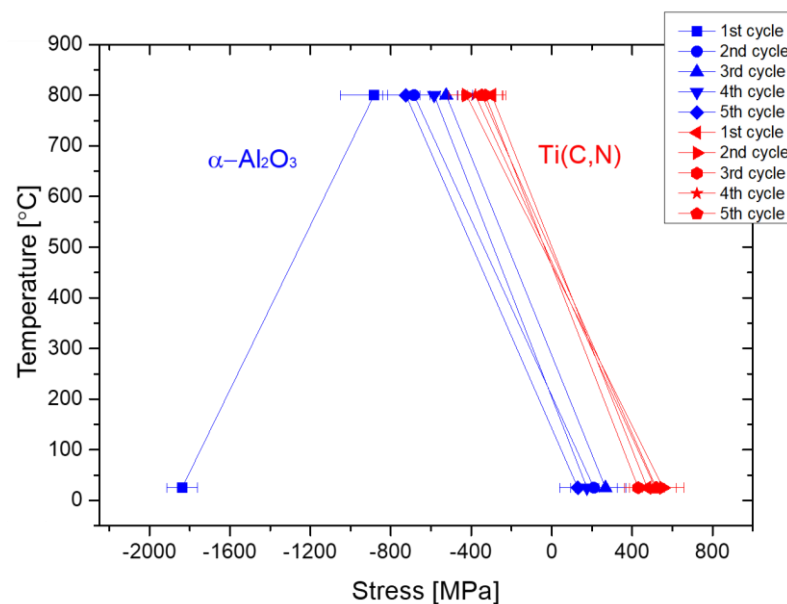


Figure 3. Stress behavior for the Ti(C,N)/ α -Al₂O₃ blasted system for 5 thermal cycles.

For the case of the intermediate Ti(C,N) layer, a different stress behavior is observed. As displayed in Figure 3, the residual stresses evolve from tensile at RT (+500 MPa) to compressive stresses at 800 °C and turn into tensile residual stresses at RT in the first thermal cycle. For the following thermal cycles (2 to 5), the stress behavior oscillates reversibly between almost the same values. Reversible stress behavior of similar Ti(C,N) wear resistant coatings for one temperature cycle has been observed in previous works of the authors [4,9,37] and more recently by Stylianou et al. on cemented carbides with different cobalt binder contents [11]. Interestingly, by interpolating the measured values, it can be estimated that the condition for zero stresses for α -Al₂O₃ is in a temperature range between 100 and 300 °C and for Ti(C,N) in a range of 500 ± 50 °C.

A further consideration is the deviation of the experimental determined stresses with the theoretical estimated ones for the system investigated, as displayed in Figure 4. For example, if the theoretical thermally induced residual stresses for both layers are calculated based on the consideration of a thin coating on an infinite bulk (using Equation (2) and the values given in Table 3), a value of +1800MPa is obtained for the Ti(C,N) layer at RT1; however, all measured values are about +500MPa. At 800 °C, the theoretical stress for Ti(C,N) is +600MPa, whereas the actual measured value is of compressive nature (−300 MPa in average). A similar discrepancy is observed in α -Al₂O₃ for both measurements at RT (+1000MPa vs. +500MPa) and 800 °C (+250MPa vs. −400MPa). This difference between experimental and theoretical stresses is understood by the formation of cooling cracks during the cooling step of the CVD process (see Figure 1), and has been discussed previously considering the variation of CTE for the coating/substrate [4,9–11], the density of cracks [4,9–11], the widening of cracks [11,38] or even the formation of subcracks during the temperature steps [10–12].

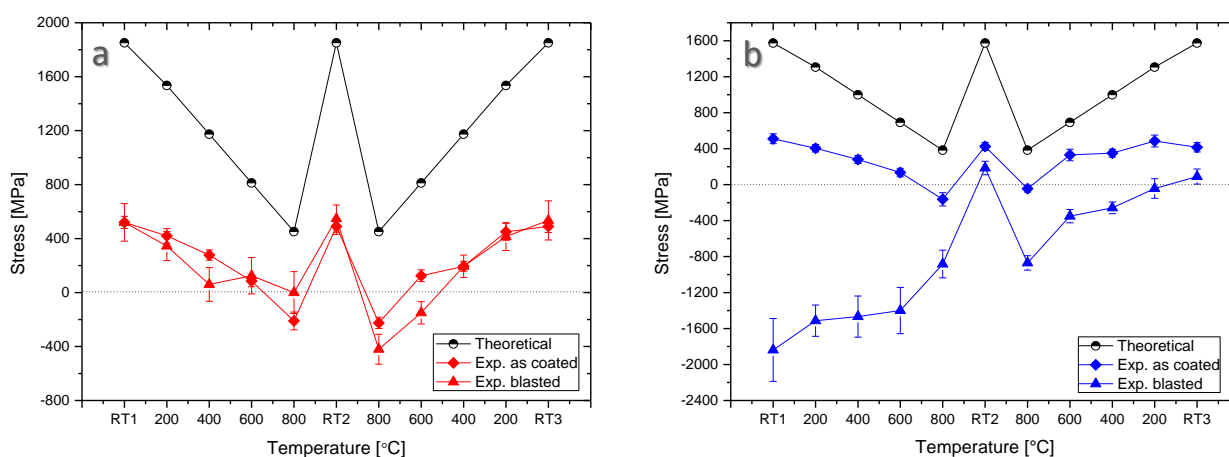


Figure 4. Experimental determined vs. theoretical calculated residual and thermal stresses for Ti(C,N) (a) and α -Al₂O₃ (b).

One remaining observation is the appearance of certain deviation from the expected linear behavior of the stress evolution at temperatures between 400 and 600 °C. This kink of stresses has been discussed with regard to the formation of additional cracks [8] or a phase transformation of the cobalt binder phase [11,12]. The latter can be a plausible explanation, since it is known that pure cobalt undergoes fcc-hcp transformation at 450 °C, and that this temperature can rise due to solid solution of tungsten in Co, which is the case for cemented carbides [2]. Furthermore, time-dependent stress analysis using in situ laser pulse heating (50 ms resolution) to simulate thermal shock conditions in WC-12% Co CVD coated samples proved the repetitive formation of compressive and tensile stresses associated with the temperature cycle and the onset of plastic deformation in both the Co and WC phases at temperatures above 750 °C [39], a fact that supports the assumption of the role of plasticity of the cemented carbide and its effect on the onset of thermal/residual stresses in the CVD layers.

3.3. TEM and XRD Microstructure Analysis

To gain further understanding of the relationship between microstructure features and their contribution to the cycling stresses observed, ex situ TEM microstructure investigations were carried out in the as-coated top-blasted condition (RT1) and after the first heating cycle (RT2). It was observed that the microstructure of the α -Al₂O₃ layer presents a high density of dislocations/defects in the near surface after top-blasting; see Figure 5. It was also observed that the density of defects is higher close to the surface of the α -Al₂O₃ top-layer, and that defects are accumulated in the basal planes of the α -Al₂O₃ grains parallel to the surface of the coated insert (Figure 6). The fact that plastic

deformation occurs during surface post-treatment on CVD α - Al_2O_3 coatings on inserts (such as particle blasting) is of considerable practical and fundamental importance. Plastic deformation takes place primarily by slip on the basal planes, which can also account for the observed anisotropy in both hardness and wear resistance observed in textured coatings. This concept has been industrially exploited to produce alumina coatings with superior resistance to brittle fracture by activating deformation at basal planes oriented parallel to the surface of the cutting insert, influencing the mechanical behavior when the α - Al_2O_3 phase works under abrasion in machining processes [40,41].

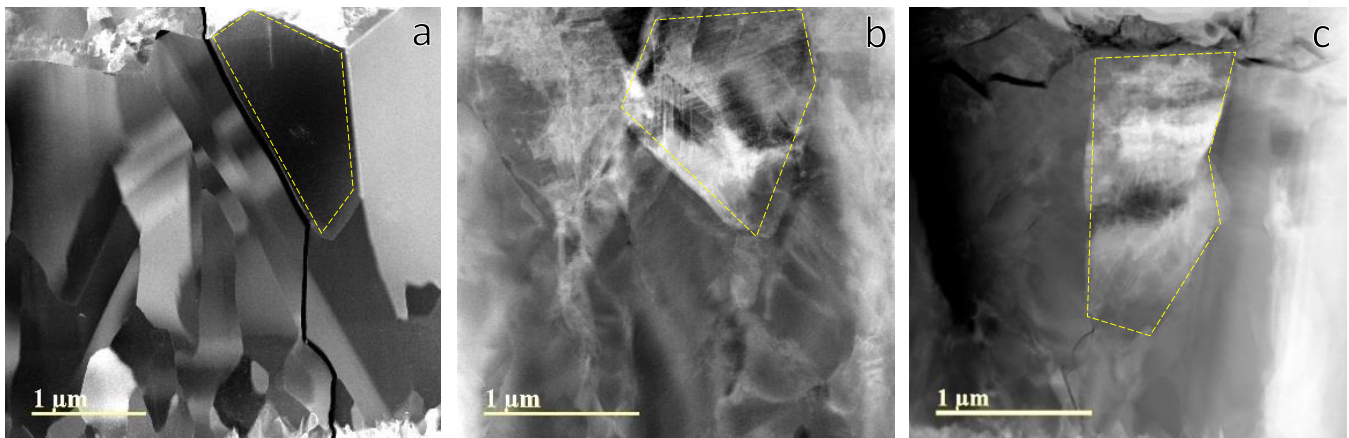


Figure 5. Dark-field scanning TEM (STEM) images of α - Al_2O_3 grains in the as-coated (a), blasted (b) and blasted then heat-treated (c) samples, with one of the grains (marked by the yellow lines) tilted to a zone axis. Growth direction is towards the top of the image.

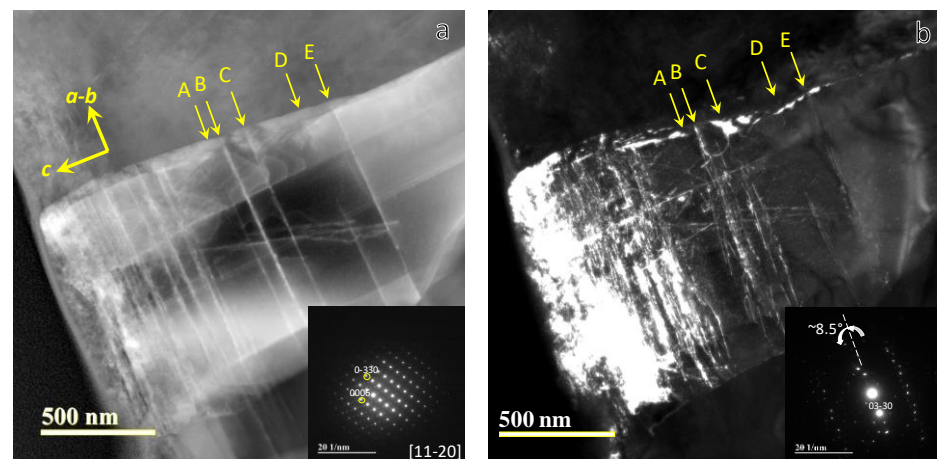


Figure 6. Dark-field STEM image (a) and weak-beam dark field (WBDF) image (b) of an α - Al_2O_3 grain in the top-blasted condition. The grain was tilted into its [11-20] zone axis for STEM imaging (a) Electron diffraction pattern (EDP shown at the bottom-right corner). White, parallel lines (for example, those marked by A–E) are seen in (a) and they are also parallel to the surface of the coating. The WBDF image was taken using the 03–30 reflection, after the grain was rotated by about 8.5° around its a-b axis from the [11-20] zone axis (see EDP inserted at bottom-right corner). Dislocation lines are seen at the locations of the lines in (a), and it became clear that the dislocation lines are lying in the basal planes.

The TEM observations show that the high energy impact of the top-blasting process stacks in the basal planes of the preferential texture of the α - Al_2O_3 layer. Furthermore, the high compressive residual stresses in the α - Al_2O_3 after top-blasting can be associated with the high density of defects in the layer, which eventually lead to a higher level of

residual stresses on the surface, and the set-up of residual stress gradients within the thickness of the thin film [5,10,42]. After the first thermal cycle, the density of defects was dramatically reduced in the α -Al₂O₃ layer (Figure 7), a fact that can contribute to the relaxation of stresses and the change to tensile residual stresses at RT. Previous reports on activation energy for stress relaxation of blasted textured Al₂O₃ (001, 012, 110) showed stress relaxation at already 400 °C in annealing experiments, with activation energies ranging between 1 and 2 eV [36], a range of temperatures similar to those used in the experiments in this work.

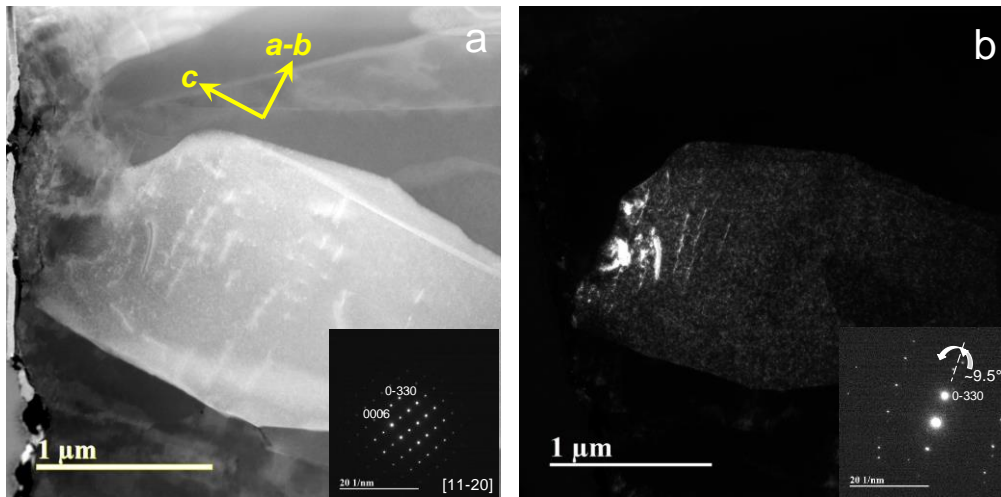


Figure 7. Dark-field STEM image (a) and weak-beam dark field (WBDF) image (b) of an α -Al₂O₃ grain in the heat-treated condition. The grain was tilted into its [11-20] zone axis for STEM imaging. White, parallel lines and line segments are seen in (a), and they lie in the basal plane which is parallel to the surface of the coating. The WBDF image was obtained using the 0-330 reflection after the grain was rotated around its a-b axis by about 9.5° from the [11-20] zone axis.

To complete the microstructural analysis, and due to the fact that the X-ray diffraction data were collected in situ to determine the coating stresses, the microstructural changes at different temperatures in the α -Al₂O₃ layer were determined by analyzing the integral width of the 012 X-ray diffraction line of this phase (Figure 8). Here, it must be recalled that in order to make the in situ measurements at varying temperatures, a limited number of inclination angles ψ was chosen, preventing the analysis of stress gradients. Hence, a diffraction line broadening caused by steep stress gradients cannot be excluded.

Additionally, the intensity of the 012 diffraction line was very small and, therefore, the effects in connection with line asymmetry were not possible to judge. Based on these boundary conditions, the results showed that the integral width of the α -Al₂O₃ 012 diffraction line decreased considerably from RT1 to 800 °C, and even more at RT2 after the first thermal cycle. This is an indication of a stepwise annihilation of defects and the corresponding change on stresses during the first thermal cycle. It can be assumed that stress relaxation proceeds by temperature activated dislocation motion by slip in the different slip systems. As early described by Hockey [43], basal slip has the lowest critical resolved shear stress at temperatures between 600 and 1000 °C, where perfect dislocations undergo dissociation allowing motion of <10–10> partial dislocations. In the subsequent thermal cycles, a slight change of integral width of the α -Al₂O₃ 012 diffraction line was observed, indicating that no considerable microstructural changes occur in the subsequent thermal cycles.

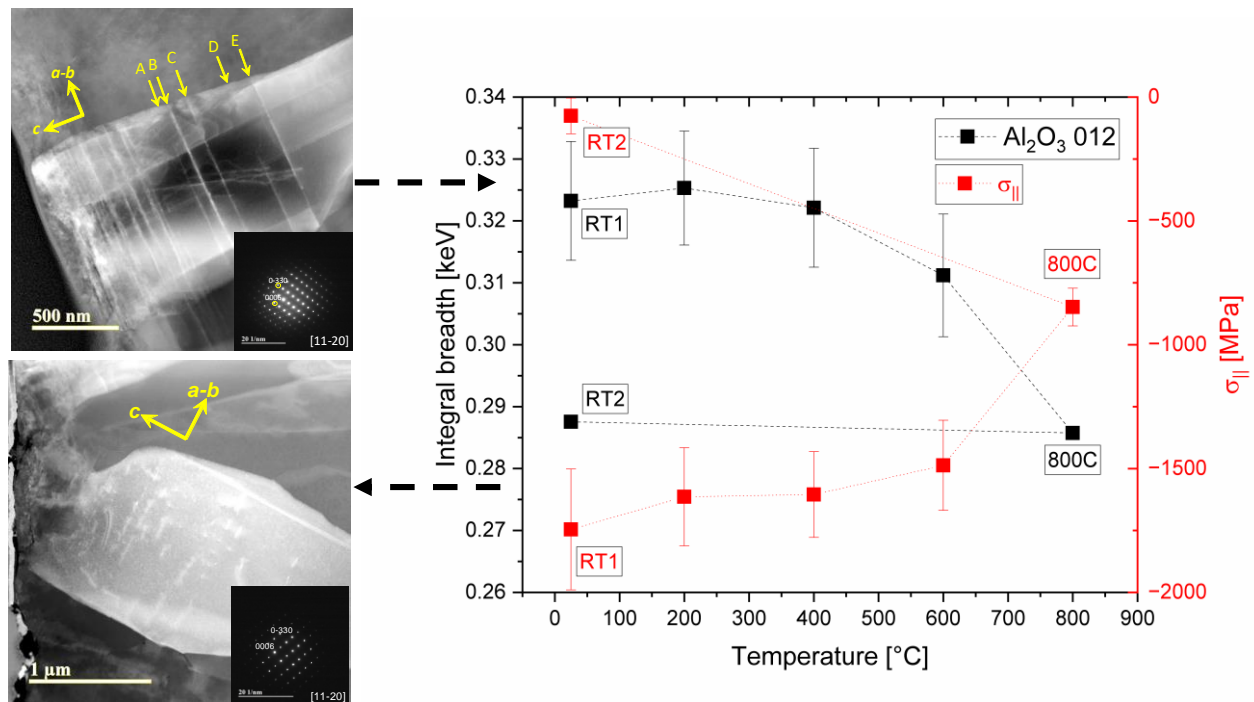


Figure 8. Left: dark-field STEM images of selected grains for the RT1 and RT2 conditions of the thermal cycle. Right: integral breadth of the 012 diffraction line of the α -Al₂O₃ phase at different temperatures and the corresponding stress values.

TEM investigations of Ti(C,N) thin films show no difference among the as-coated, top-blasted and heat treated conditions. Mainly stacking faults and twin boundaries defects for all conditions were observed, as displayed in Figures 9 and 10. This corroborates that the top-blasting process in α -Al₂O₃/Ti(C,N) multilayer CVD coatings is mainly confined to the α -Al₂O₃ top-layer. Though, in previous works on top-blasted TiN [8] and Ti(C,N) [9] CVD layers (without top α -Al₂O₃ layers on it), a strong change in defect density and residual stress at RT were observed. The stresses induced by top-blasting were annealed upon heating, indicating that Ti(C,N) may undergo a similar mechanism—as observed for the α -Al₂O₃ in this work if defect introduction by mechanical impact is possible.

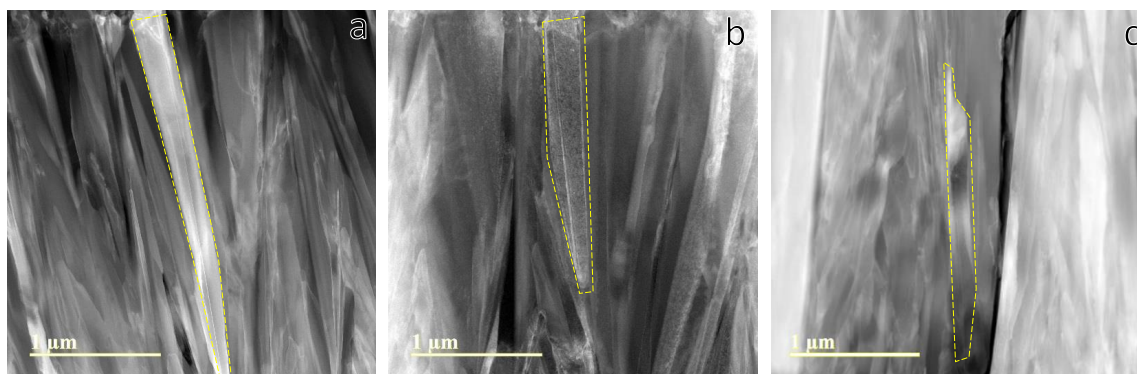


Figure 9. Dark-field STEM images of Ti(C,N) grains in the as-coated (a), blasted (b) and blasted then heat-treated (c) samples, with one of the grains (marked by the yellow lines) tilted to a zone axis. The growth direction is towards the top of the image.

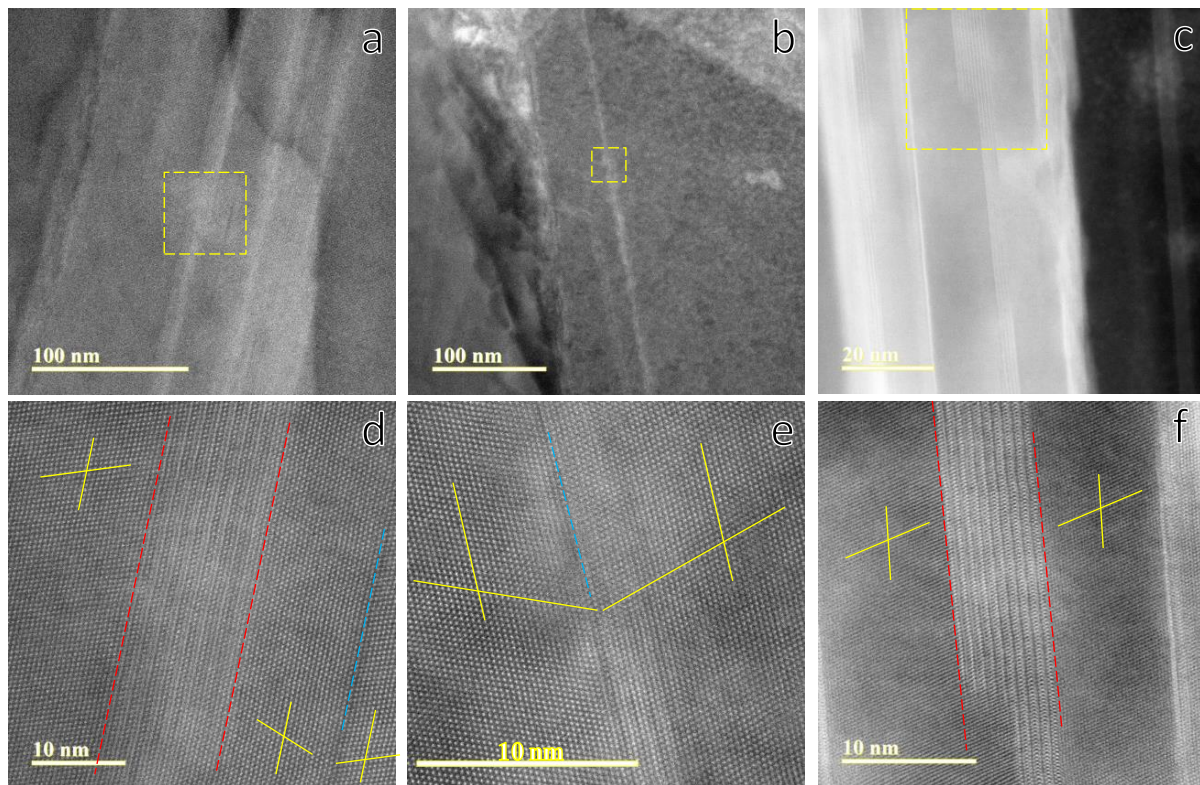


Figure 10. Dark-field STEM images Ti(C,N) grains. HR-TEM of framed areas in (a–c) are shown in (d–f), respectively. Yellow solid lines and the cyan dashed lines mark the (111) planes and the twin boundaries. Stacking faults are present between the red dashed lines. (a,d): as-coated, (b,e): blasted, (c,f): blasted then heat-treated.

The integral breadth of the 200 diffraction line of the Ti(C,N) layer (in the top-blasted condition) was analyzed at different stages of the heating cycle. It was observed that the integral breadth shows no significant change at any temperature. Furthermore, the calculation of the microstrain resulted in an almost constant value for all temperatures, indicating that the change of the residual stresses during the heat cycles is not correlated to changes in the defect density of the carbonitride lattice. For the temperature range investigated, it can be concluded that the observed change of residual stresses is not accompanied by defect creation or annihilation (Figure 11).

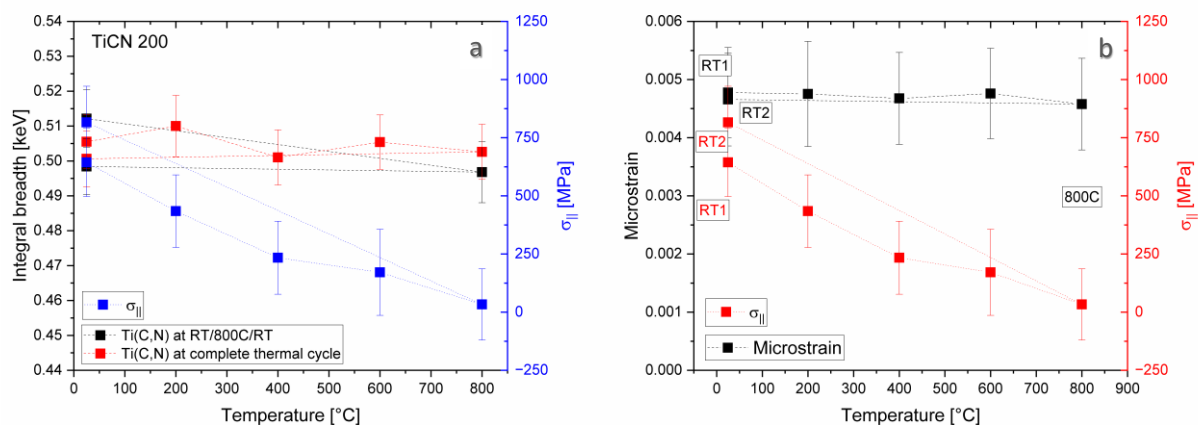


Figure 11. In situ determined (a) Integral breadth and (b) microstrain of the 200 diffraction line of the Ti(C,N) phase at different temperatures for one thermal cycle. Reversible stresses are not associated with microstructural changes in Ti(C,N) phase.

Hence, in response to the heat treatment, the system has an elastic behavior in terms of the deformation response. Consequently, the observed residual stresses are solely the result of the difference in CTE between the Ti(C,N) layer and the cemented carbide substrate.

As a summary, a phenomenological model for the observed stress evolution linked to the cycling temperature is presented (Figure 12). It is worth mentioning that more than 50 samples with similar characteristics have been studied by this research group, and that the stress behavior presents similar characteristics with the model summarized in this work. Top-blasting induces high compressive stresses in the α -Al₂O₃ layer associated with plastic deformation of the alumina grains (as shown in the STEM images). The thermal stress evolution of the top-blasted α -Al₂O₃ layer is accompanied by annihilation of defects and relaxation by a thermally activated process. Such stress relaxation can be correlated to defect configurations and recombination mechanisms that influence the activation energy for defect annihilation and stress reduction. A similar phenomenon has been observed for thin films deposited by arc-evaporation [44], where the high intrinsic compressive stresses induced by ion-peening (in the order of -5 GPa) are relaxed to -1 GPa upon annealing at 900 °C. In this study, most defects introduced by top-blasting are released in the 1st thermal cycle, and the remaining defects in the subsequent cycles—as observed in the stress change/evolution—are released until an elastic response condition associated with the thermal fluctuations is set.

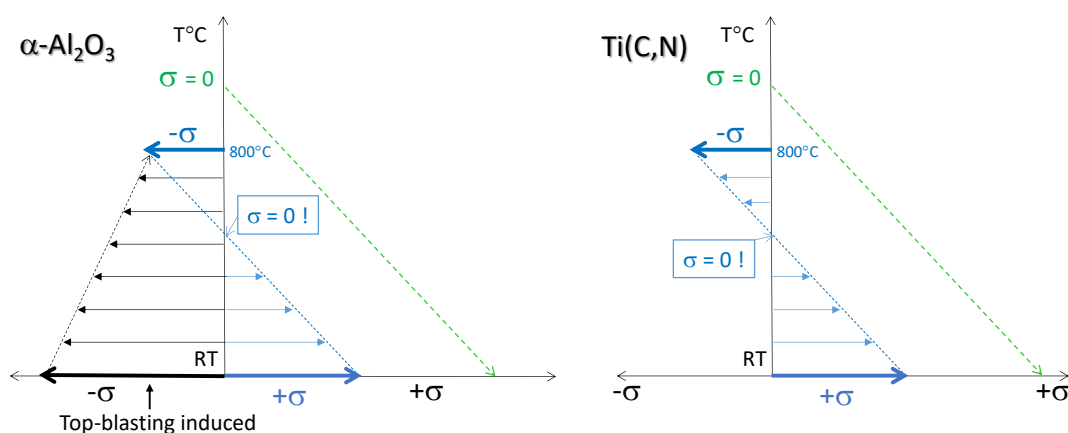


Figure 12. Phenomenological model for the stress evolution of α -Al₂O₃ coating and Ti(C,N) layers based on collected experimental data. Estimated residual and thermal stresses (dark and blue lines); theoretical thermal stress evolution (green line) considering $\sigma = 0$ at the deposition temperature is displayed. The top-blasted α -Al₂O₃ layer presents two stages: top-blasted-induced compressive stresses (dark line) reduced in first temperature step, and reversible stress behavior (blue line) in the following cycles. The Ti(C,N) stresses show a tensile–compressive–tensile behavior over all investigated temperature cycles.

For the Ti(C,N) layer, no effect of top-blasting in the residual stress behavior of the layer was observed; hence, the cycling stresses evolved reversibly following the temperature cycle, from tensile (at RT1) to compressive (at high T) to tensile (at RT2). However, this change of stresses was not connected to any microstructural change, as determined by the TEM investigations and the in situ analysis of defect evolution by XRD. The evolved compressive stresses at high temperatures are in the order of magnitude of -400 MPa, far below the reported compressive strength of polycrystalline Ti(C,N), 16 GPa [45] and single crystal α -Al₂O₃, 31 GPa [46], respectively, indicating that the elastic deformation behavior for the thin films is plausible.

This model does not consider steep stress gradients in the CVD layers (as it may be present in the top-blasted α -Al₂O₃ layer) and possible stress compensations due to the presence of the bonding layer between the α -Al₂O₃ and Ti(C,N) layer. The authors of this work showed that stress gradients can arise due to chemical variations within the CVD layer [15], or because of different layer thickness and the response to top blasting [47].

In our investigations, we did not observe a significant curvature in the $d_{\psi}^{hkl} - \sin^2 \psi$ —plots, which would indicate the occurrence of steep stress gradients. This finding can be explained by the low absorption of alumina and the small thickness D of the layer. In such cases, the X-ray penetration depth $\tau_{1/e}$ is much larger than D , which results in almost linear $d_{\psi}^{hkl} - \sin^2 \psi$ —distributions up to very large inclination angles (i.e., grazing diffraction conditions) [48].

Furthermore, it has been discussed that for multilayer systems consisting of a stack of thin sublayers, the stress analysis becomes sophisticated [49]. By fitting appropriate models to the $d - \sin^2 \psi$ plots that include the stack geometry, the parameters which describe the stress depth profiles within the individual sublayers can be estimated. In this case, it is plausible that the bonding layer acts as a stress compensation layer for the high compressive stresses in the top-blasted $\alpha\text{-Al}_2\text{O}_3$ layer. This—together with the steep gradients—could explain the large difference in the averaged stress between the Ti(C,N) and the $\alpha\text{-Al}_2\text{O}_3$ layers observed in this work.

Another interesting fact is that the condition for zero stresses of the Ti(C,N)/ $\alpha\text{-Al}_2\text{O}_3$ system is set at a temperature range between 300 and 500 °C. If it is considered that in interrupted milling machining, the common temperature jumps are in the range 200–600 °C [50], this may indicate that the observed reversible changes of thermal stresses (tensile–compressive–tensile stress cycles) are a favorable condition for opening, propagation and widening of the initial microcracks, a fact that can contribute to the formation and propagation of comb crack wear in milling inserts. Finally, the role of the cemented carbide substrate was not addressed in this work, and the assumption of binder phase temperature-dependent plastic deformation remains a task for future investigations.

4. Conclusions

The results of this work are intended to contribute to understanding the interplay between the microstructural changes and the evolution of stresses in Ti(C,N)/ $\alpha\text{-Al}_2\text{O}_3$ coatings by combining in situ high energy X-ray diffraction experiments and TEM microstructural analysis.

Main conclusions:

- The introduction of high compressive stresses in $\alpha\text{-Al}_2\text{O}_3$ by top-blasting is connected to a high defect density at the basal planes of the alumina layer, as shown in the TEM image analysis.
- Upon thermal cycling, the measured stress relaxation in $\alpha\text{-Al}_2\text{O}_3$ is due to annihilation of defects, as observed by the reduction in integral breadth for the 012 diffraction line as well as the contrast change in the dark-field STEM analysis.
- By increasing the number of cycles, a reversible temperature-dependent stress condition in the $\alpha\text{-Al}_2\text{O}_3$ layer is achieved.
- Top-blasting does not affect the initial microstructure and residual stress of the Ti(C,N) layer.
- The Ti(C,N) layer shows a temperature-dependent reversible cycling behavior and an elastic deformation behavior in the temperature range investigated.
- Observed deviations between theoretical stresses and measured stresses can be associated with microcrack formation during the cooling step in the CVD process.
- The zero stress condition for the temperature-dependent reversible stress behavior of the Ti(C,N)/ $\alpha\text{-Al}_2\text{O}_3$ system sets at a temperature between 300 and 500 °C, which is a favorable condition that can contribute to the formation and propagation of thermomechanical cracks in, e.g., milling inserts.
- The results show that the matching of CTE between the substrate and coating is crucial to reduce cycling stresses that promotes crack propagation. Technically, this could be achieved by cemented carbide substrates with higher CTE (by, for example, increasing the binder content) or by layers with low CTE, such as Zr(C,N) or Hf(C,N). This, alongside tailored top-blasting parameters, is crucial for delaying crack opening in interrupted machining operations.

Based on the results of this work, other systems are under investigation with the aim of tailoring the residual stress behavior of CVD multilayers working at cycling thermomechanical loads.

Author Contributions: Conceptualization, J.G. and M.M. (Maiara Moreno); methodology, W.W., D.A., M.M. (Matthias Meixner), M.K. and C.G.; formal analysis and investigation, J.G., M.M. (Maiara Moreno), W.W., D.A., M.K., M.M. (Matthias Meixner) and C.G.; writing—original draft preparation, J.G. and M.M. (Maiara Moreno); writing—review and editing, J.G., M.M. (Maiara Moreno), W.W., D.A., M.K., M.M. (Matthias Meixner) and C.G.; supervision, J.G.; project administration, J.G. and H.P.; funding acquisition, J.G. and H.P. All authors have read and agreed to the published version of the manuscript.

Funding: This research was funded by EUROPEAN UNION'S HORIZON 2020 research and innovation program, grant number 644013 (CREATE-Network).

Institutional Review Board Statement: Not applicable.

Informed Consent Statement: Not applicable.

Data Availability Statement: The data presented in this study are available on request from the corresponding author. The data are not publicly available.

Acknowledgments: The authors thank Sandvik Coromant R&D colleagues Martina Lattemann and Ernesto Coronel for assistance in TEM sample preparation and Raluca Morjan Brenning and Jeanette Persson for the production of tailored CVD coated samples.

Conflicts of Interest: The authors declare no conflict of interest. The funders had no role in the design of the study, in the collection, analyses, or interpretation of data, in the writing of the manuscript, and in the decision to publish the results.

References

1. Sadik, I. *An Introduction to Cutting Tools Materials and Applications*; Elanders: Mölndal, Sweden, 2013; ISBN 978-91-637-4920-9.
2. García, J.; Collado Cipres, V.; Blomqvist, A.; Kaplan, B. Cemented carbide microstructures: A review. *Int. J. Ref. Met. Hard Mater.* **2019**, *80*, 40–68. [[CrossRef](#)]
3. Mitterer, C. PVD and CVD Hard Coatings. *Encyclopedia Comprehensive Hard Materials*; Elsevier Ltd.: Amsterdam, The Netherlands, 2014; Volume 2, pp. 449–467.
4. García, J.; Moreno, M.; Östby, J.; Persson, J.; Pinto, H. Design of coated cemented carbide with improved comb crack resistance. In Proceedings of the Plansee Seminar 2017, Reutte, Austria, 29 May–2 June 2017.
5. Klaus, M.; Genzel, C.; Holzschuh, H. Residual stress depth profiling in complex hard coating systems by X-ray diffraction. *Thin Solid Films* **2008**, *517*, 1172–1176. [[CrossRef](#)]
6. Schalk, N.; Mitterer, C.; Czettel, C.; Sartory, B.; Penoy, M.; Michotte, C. Dry blasting of alpha and kappa-Al₂O₃ CVD hard coatings: Friction behavior and thermal stress relaxation. *Tribol. Lett.* **2013**, *52*, 147–154. [[CrossRef](#)]
7. Teppernegg, T.; Klünsner, T.; Angerer, P.; Tritremmel, C.; Czettel, C.; Keckes, J.; Ebner, R.; Pippan, R. Evolution of residual stress and damage in coated hard metal milling inserts over the complete tool life. *Int. J. Ref. Met. Hard Mater.* **2014**, *47*, 80–85. [[CrossRef](#)]
8. Bartosik, M.; Pitonak, R.; Keckes, J. In Situ High Temperature X-Ray Diffraction Reveals Residual Stress Depth Profiles in Blasted TiN Hard Coatings. *Adv. Eng. Mat.* **2011**, *13*, 705–711. [[CrossRef](#)]
9. García, J.; Pinto, H.; Ramos-Moore, E.; Espinoza, C.; Östby, J.; Coelho, R. In-situ high temperature stress analysis of Ti(C,N) coatings on functionally graded cemented carbides by energy dispersive synchrotron X-ray diffraction. *Int. J. Ref. Met. Hard Mater.* **2016**, *56*, 27–34. [[CrossRef](#)]
10. Faksa, L.; Daves, W.; Ecker, W.; Klünsner, T.; Tkadletz, M.; Czettel, C. Effect of shot peening on residual stresses and crack closure in CVD coated hard metal cutting inserts. *Int. J. Ref. Met. Hard Mater.* **2019**, *82*, 174–182. [[CrossRef](#)]
11. Stylianou, R.; Velic, D.; Daves, W.; Ecker, W.; Stark, A.; Schell, N.; Tkadletz, M.; Schalk, N.; Czettel, C.; Mitterer, C. Stress relaxation through thermal crack formation in CVD TiCN coatings grown on WC-Co with different Co contents. *Int. J. Ref. Met. Hard Mater.* **2020**, *86*, 105012. [[CrossRef](#)]
12. Stylianou, R.; Velic, D.; Daves, W.; Ecker, W.; Tkadletz, M.; Schalk, N.; Czettel, C.; Mitterer, C. Thermal crack formation in Ti(C,N)/Al₂O₃ bilayer coatings grown by thermal CVD WC-Co substrates with varied Co content. *Surf Coat Techn.* **2020**, *392*, 125687. [[CrossRef](#)]
13. Genzel, C.; Denks, I.A.; Gibmeier, J.; Klaus, M.; Wagener, G. The materials science synchrotron beamline EDDI for energy-dispersive diffraction analysis, Nuclear Instruments and Methods. In *Physics Research Section A: Accelerators, Spectrometers, Detectors and associated Equipment*; Elsevier: Amsterdam, The Netherlands, 2007; Volume 578, pp. 23–33.
14. Klaus, M.; Garcia-Moreno, F. The 7T-MPW-EDDI Beamline at Bessy II. *J. Large Scale Res. Facil.* **2016**, *2*, A40. [[CrossRef](#)]

15. Klaus, M.; Genzel, C.; García, J. Nondestructive separation of residual stress and composition gradients in thin films by angle- and energy-dispersive X-ray diffraction. II. Experimental validation. *J. Appl. Cryst.* **2017**, *50*, 265–277. [[CrossRef](#)]
16. Stefanelli, M.; Todt, J.; Riedl, A.; Ecker, W.; Müller, T.; Daniel, R.; Burghammer, M.; Keckes, J. X-ray analysis of residual stress gradients in TiN coatings by Laplace space approach and cross sectional nanodiffraction: A critical comparison. *J. Appl. Cryst.* **2013**, *46*, 1378–1385. [[CrossRef](#)]
17. Noyan, I.C.; Huang, T.C.; York, B.R. Residual stress/strain analysis in thin films by X-ray diffraction. *Crit. Rev. Solid State Mater. Sci.* **1995**, *20*, 125–177. [[CrossRef](#)]
18. Noyan, I.C.; Cohen, J.B. *Residual Stress: Measurement by Diffraction and Interpretation*; Springer: Berlin/Heidelberg, Germany, 1987.
19. Macherauch, E.; Müller, P. Das $\sin^2\psi$ -Verfahren der röntgenographischen Spannungsmessung. *Z. Angew. Physik* **1961**, *13*, 305–312.
20. Eshelby, J.D. The Determination of the Elastic Field of an Ellipsoidal Inclusion, and Related Problems. *Proc. Roy. Soc.* **1957**, *A241*, 376–396.
21. Kröner, E. Berechnung der elastischen Konstanten des Vielkristalls aus den Konstanten des Einkristalls. *Z. Physik* **1958**, *151*, 504–518. [[CrossRef](#)]
22. Gao, C.; Zhao, Z.; Li, Z. Modeling of thermal stresses in elastic multilayer coating systems. *J. Appl. Phys.* **2015**, *117*, 055305. [[CrossRef](#)]
23. El Azhari, I.; García, J.; Soldera, F.; Suarez, S.; Jiménez-Piqué, E.; Mücklich, F.; Llanes, L. Contact damage investigation of CVD carbonitride hard coatings deposited on cemented carbides. *Int. J. Ref. Met. Hard Mater.* **2020**, *86*, 105050. [[CrossRef](#)]
24. Rупpi, S.; Larsson, A.; Flink, A. Nanoindentation hardness, texture and microstructure of α -Al₂O₃ and κ -Al₂O₃ coatings. *Thin Solid Films* **2008**, *516*, 5959–5966. [[CrossRef](#)]
25. Friedrich, C.; Berg, G.; Broszeit, E.; Berger, C. Datensammlung zu Hartstoffeigenschaften. *Mater. Werkst.* **1997**, *28*, 59–76. [[CrossRef](#)]
26. Wachtman, J.B.; Scuderi, T.G.; Cleek, G.W. Linear thermal expansion of aluminium oxide. *J. Am. Ceram. Soc.* **1961**, *10*, 319–323.
27. Kral, C.; Lengauer, W.; Rafaja, D.; Etmayer, P. Critical review on the elastic properties of transition metal carbides, nitrides and carbonitrides. *J. Alloys Compd.* **1998**, *265*, 215–233. [[CrossRef](#)]
28. Aigner, K.; Lengauer, W.; Rafaja, D.; Etmayer, P. Lattice parameters and thermal expansion of Ti(C_xN_{1-x}), Zr(C_xN_{1-x}), Hf(C_xN_{1-x}) and TiN_{1-x} from 298 to 1473 K as investigated by high-temperature X-ray diffraction. *J. Alloys Compd.* **1994**, *215*, 121–126. [[CrossRef](#)]
29. Halvarsson, M.; Langer, V.; Vuorinen, S. Determination of the thermal expansion of α -Al₂O₃ by high temperature XRD. *Surf. Coat. Technol.* **1995**, *76–77*, 358–362. [[CrossRef](#)]
30. De Keijser, T.H.; Langford, J.I.; Mittemeijer, E.J.; Vogels, A.B.P. Use of the Voigt function in a single-line method for the analysis of X-ray diffraction line broadening. *J. Appl. Cryst.* **1982**, *15*, 308–314. [[CrossRef](#)]
31. Delhez, R.; De Keijser, T.H.; Mittemeijer, E.J. Determination of crystallite size and lattice distortions through X-ray diffraction line profile analysis. *Fresenius Z. Anal. Chem.* **1982**, *312*, 1–16. [[CrossRef](#)]
32. Apel, D.; Klaus, M.; Genzel, C.; Balzar, D. Rietveld refinement of energy-dispersive synchrotron measurements. *Z. Krist.* **2011**, *226*, 934–943. [[CrossRef](#)]
33. Rojas, D.; Garcia, J.; Prat, O.; Agudo, L.; Carrasco, C.; Kaysser-Pyzalla, A.R. Effect of processing parameters on the evolution of dislocation density and sub-grain size of a 12% Cr heat resistant steel during creep at 650° C. *Mater. Sci. Eng. A* **2011**, *528*, 1372–1381. [[CrossRef](#)]
34. Gassner, M.; Schalk, N.; Tkadletz, M.; Czettel, C.; Mitterer, C. Thermal crack network on CVD TiCN/ α -Al₂O₃ coated cemented carbide cutting tools. *Int. J. Ref. Met. Hard Mater.* **2019**, *81*, 1–6. [[CrossRef](#)]
35. Barbatti, C.; García, J.; Pinto, H.; Kostka, A.; Di Prinzio, A.; Staia, M.; Pitonak, R.; Pyzalla, A. Influence of micro-blasting on the microstructure and residual stresses of CVD κ -Al₂O₃ coatings. *Surf. Coat. Technol.* **2009**, *203*, 3708–3717. [[CrossRef](#)]
36. Ekström, E. Effect of texture and blasting pressure on residual stresses and surface modifications in wet sand blasted α -Al₂O₃ coating. Master's Thesis, Linköping University, Linköping, Sweden, 2015.
37. Ramos-Moore, E.; Espinoza, C.; Coelho, R.; Pinto, H.; Brito, P.; Soldera, F.; Mücklich, F.; García, J. Investigations on thermal stresses of a graded Ti (C, N) coating deposited on WC-Co hardmetal. *Adv. Mater. Res.* **2014**, *996*, 848–854. [[CrossRef](#)]
38. Chien, H.; Diaz-Jimenez, C.; Rohrer, G.S.; Ban, Z.; Prichard, P.; Liu, Y. The influence of residual thermal stresses on the mechanical properties of multilayer -Al₂O₃ /TiC_xN_{1-x} coatings on WC/Co cutting tools. *Surf. Coat. Technol.* **2013**, *215*, 119–126. [[CrossRef](#)]
39. Gruber, D.P.; Kiefer, D.; Rössler, R.; Beckmann, F.; Tkadletz, M.; Klünsner, T.; Czettel, C.; Keckes, J.; Gibmeier, J. 20 Hz synchrotron Z-ray diffraction analysis in laser-pulsed WC-Co hard metal reveals oscillatory stresses and reversible composite plastification. *Int. J. Ref. Met. Hard Mater.* **2019**, *82*, 121–128. [[CrossRef](#)]
40. Rупpi, S. Cemented carbide body with high wear resistance and extra tough behavior. U.S. Patent 2000/6015614 A1, 18 January 2000.
41. Rупpi, S. Enhanced performance of α -Al₂O₃ coatings by control of crystal orientation. *Surf. Coat. Technol.* **2008**, *202*, 4257–4269. [[CrossRef](#)]
42. Tkadletz, M.; Keckes, J.; Schalk, N.; Krajinovic, I.; Burghammer, M.; Czettel, C.; Mitterer, C. Residual stress gradients in α -Al₂O₃ hard coatings determined by pencil-beam X-ray nano-diffraction: The influence of blasting media. *Surf. Coat. Technol.* **2015**, *262*, 134–140. [[CrossRef](#)]
43. Hockey, B. Plastic deformation of aluminum oxide by indentation and abrasion. *J. Am. Ceram. Soc.* **1971**, *54*, 223–231. [[CrossRef](#)]

44. Karlsson, L.; Hörling, A.; Johansson, M.P.; Hultman, L.; Ramanath, G. The influence of thermal annealing on residual stresses and mechanical properties of arc-evaporated $\text{TiC}_x\text{N}_{1-x}$ ($X = 0, 0.15$ and 0.45) thin films. *Acta Mater.* **2002**, *50*, 5103–5114. [[CrossRef](#)]
45. El Azhari, I.; Garcia, J.; Zamanzade, M.; Soldera, F.; Pauly, C.; Llanes, L.; Mücklich, F. Investigations on micro-mechanical properties of polycrystalline Ti(C,N) and Zr(C,N) coatings. *Acta Mater.* **2018**, *149*, 364–376. [[CrossRef](#)]
46. Riley, F.L. *Structural Ceramics: Fundamentals and Case Studies*; Cambridge University Press: Cambridge, UK, 2009.
47. Klaus, M.; Genzel, C. Multilayer Systems for Cutting Tools: On the Relationship between Coating Design, Surface Processing, and Residual Stress. *Adv. Eng. Mater.* **2011**, *13*, 845–850. [[CrossRef](#)]
48. Genzel, C. X-Ray Stress Gradient Analysis in Thin Layers—Problems and Attempts at Their Solution. *Phys. Stat. Sol. A* **1997**, *159*, 283–296. [[CrossRef](#)]
49. Klaus, M.; Denks, I.A.; Genzel, C. X-Ray Diffraction Analysis of Nonuniform Residual Stress Fields $\sigma_{ij}(\tau)$ under Difficult Conditions. *Mater. Sci. Forum* **2006**, *524–525*, 601–606. [[CrossRef](#)]
50. AB Sandvik Coromant. *Measurement and Modeling of Temperature Fluctuations in Milling Operations*; AB Sandvik Coromant: Sandviken, Sweden, 2019.